CHAPTER

19

A Numerical Study of Epithermal Neutron Log Response and Application of Image Log for Porosity Determination

Swagato Dasgupta[*], *Troyee Dasgupta*[†], *Vir Narayan Singh*[‡], *Soumyajit Mukherjee*[§]

[*]Landmark Software Solutions, Halliburton, Bangalore, India [†]Exploration Division, Reliance Industries Ltd., Navi Mumbai, India [‡]131-A, Shakumbari Enclave, Delhi Road, Roorkee, India [§]Department of Earth Sciences, Indian Institute of Technology Bombay, Powai, Mumbai, India

OUTLINE

1 INTRODUCTION

Understanding the reservoir heterogeneity in terms of porosity and permeability is a key concern in many producing, developed, and discovered fields worldwide (Bansal et al., 2004; Pranter et al., 2006; Fitch et al., 2013). Among different petrophysical logs used for formation evaluation, neutron logs provide direct measurement of reservoir porosity. Other logs from where porosity data can be derived are density and sonic logs. Reservoir porosity is of two types, viz., primary and secondary (Serra, 1984; Singhal and Gupta, 2010; Anovitz and Cole, 2015). Primary porosity is the intergranular porosity, which can be directly obtained from porosity logs (e.g., neutron log). Secondary porosity is related to grain leeching, vugs, caverns, and in many cases produced by natural fractures (Bratton et al., 2006). It is sometimes difficult to recognize from conventional porosity logs. Image logs (like Formation Micro–Imager) identify

different structural and morphological features that result in secondary porosity generation, thus there is an added advantage for deciphering the reservoir heterogeneity related to secondary porosity generation This chapter provides fundamentals of an epithermal neutron log in detecting primary porosity of formation. Moreover, it also highlights the benefits of an image log in identification of fracture related to secondary porosity that the conventional porosity logs often fail to detect.

Neutron logs are porosity logs that measure the hydrogen ion concentration in a formation. In clean formations (i.e., shale-free) where water or oil fills up the pore spaces, the neutron log measures the liquid-filled porosity. When a beam of high-energy neutrons is sent into the formation, neutrons slow down when they collide with nuclei as per the neutron diffusion (Liverhant, 1960; Neuman et al., 1988). In neutron logging, the formation surrounding the borehole is bombarded by a beam of fast neutrons from a suitable source such as the Americium-Beryllium (Am-Be) source. The life span of these neutrons, after leaving the source and interacting with the surrounding media, becoming slowed down and finally captured by nuclei, can be divided into four phases: (i) fast, (ii) slowing down, (iii) diffusion, and (iv) capture. The maximum amount of energy loss is a function of formation's hydrogen concentration, because hydrogen atomic mass is almost equal to that of a neutron. Neutron logging tools are of different types such as the epithermal neutron tool, thermal neutron tool, and compensated neutron logging tool. This depends upon various factors, that is, the differences in source and detector types, spacing between source and detector, borehole effect, etc. (Lynch, 1962; Serra, 1984; Schlumberger Log Interpretation Principles/Applications, 1989).

As the collision between the neutrons and the formation nuclei continues, the cloud of neutrons either spreads or diffuses into the formation. Neutrons generally obey a diffusion equation, which describes the conservation of neutrons (Glasstone and Edlund, 1957):

$$\text{Production} + \text{Scattering} - \text{Absorption} - \text{Leakage} = 0 \tag{1}$$

In the present study, the general equation of elementary diffusion theory is solved for selected cases of cylindrical geometry, which occurs in real well logging scenario.

2 COMPUTATION AND RESULT

The application of one-group diffusion theory to the slowing down of neutrons results in a distribution of epithermal neutrons (Glascock, 2006; Tittle, 1961) in hydrogenous media. This condition is applied for a fast neutron point source on the axis of two concentric cylinders of finite radius and infinite length (Tittle, 1961). Tittle (1961) presented the solution of the diffusion equation when a borehole is surrounded by another rock, which extends laterally. The situation is modeled here as consisting of two concentric cylinders, with the inner cylinder representing the borehole with a finite radius. This has been called a concentric cylindrical medium (Fig. 1). The concentric cylinders are considered to be of infinite length with the source on the axis. The inner cylinder represents the borehole, which is taken to be water-filled. The effect of the logging instrument in displacing the fluid is neglected. Although the outer cylinder may be of infinite radius, we presume a finite radius because it is easier to deal with. The radius of the inner cylinder is taken as "a" and that of outer cylinder as "b". The latter value includes the extrapolation distance (Fig. 1; Tittle, 1961; Allen and Tittle, 1964; Tittle and Allen, 1966).

A synthetic epithermal neutron log is generated by numerically simulating the neutron diffusion process by using one group diffusion theory in the case of two concentric cylindrical mediums, that is, for the borehole and the invasion zone. The numerical simulation of epithermal neutron log done deterministically is insensitive to the strong thermal absorbers, which otherwise perturb the thermal neutron response (Tittle, 1961; Tittle and Allen, 1966). An equation of neutron flux is obtained for a concentric cylindrical medium. Finally, synthetic epithermal neutron porosity logs are produced for clean sandstone and limestone formations at different ranges of water saturation levels.

Neutrons generally obey the steady state equation for the entire region excluding the neutron point source (Glasstone and Edlund, 1957; Tittle, 1961):

$$D(\nabla)^2\Phi - \Phi/\lambda_a + S = \partial n/\partial t \tag{2}$$

where Φ: neutron flux ($\Phi = nv$; n: number of neutrons; v: neutron speed), D: neutron diffusion coefficient; λ_a: absorption mean-free path. We are specifically interested in the point source. Therefore at all points except the origin, the source term (S) is zero. Thus Eq. (2) becomes (Tittle, 1961):

$$\nabla^2\Phi - \Phi/L_s{}^2 = 0 \tag{3}$$

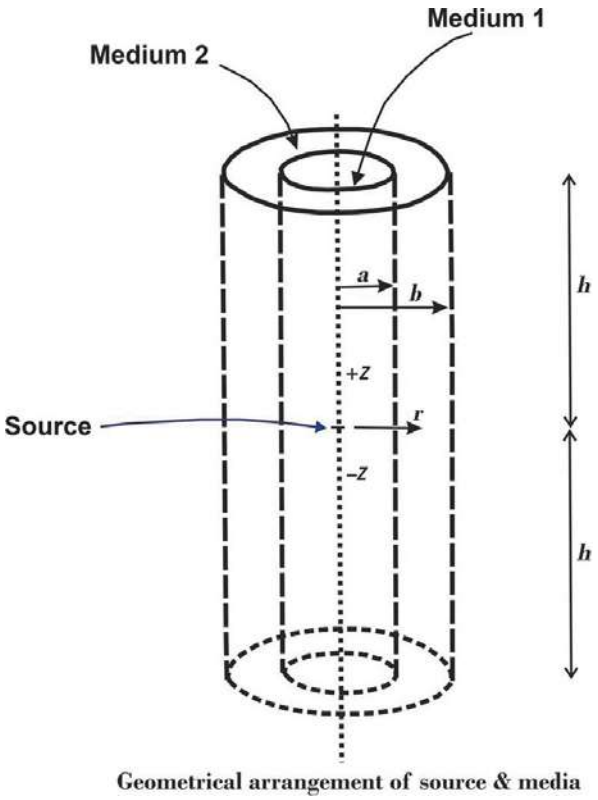

FIG. 1 Schematic diagram depicting geometric arrangements of neutron source and concentric cylindrical medium; the borehole is the inner cylinder having radius "*a*" (medium 1) whereas the invasion zone is the outer cylinder with radius "*b*" (medium 2). The source is located at the central axis of the concentric cylinders.

Here $L_s = (\lambda_a D)^{0.5}$.

Eq. (3) is applied in each medium, but L_s differs for the two media, that is, L_1 for the inner and L_2 for the outer cylinder (Tittle and Allen, 1966). Therefore:

$$\nabla^2 \Phi_1 - \Phi_1 / {L_1}^2 = 0; \;\; 0 \le r \le a \tag{4}$$

$$\nabla^2 \Phi_2 - \Phi_2 / {L_2}^2 = 0; \;\; a \le r \le b. \tag{5}$$

These equations are solved in a cylindrical medium using the Bessel Function to deduce the flux for both inner and outer cylinder and thus the total flux in case of concentric cylinders (details found in the Appendix).

To simulate the epithermal neutron log, the following assumptions are made:

(i) The clean formation is either sandstone or limestone with pore spaces filled with water and/or gas (CH_4). As the natural gas consists almost >80% of CH_4 in pore space (Burruss and Ryder, 2003; Yang, 2017), only this gas is considered.
(ii) Clean sandstone is composed of mineralogically pure quartz (SiO_2). Pure limestone consists of only calcium carbonate ($CaCO_3$).
(iii) The borehole is filled with water devoid of mud-cake. Neutron flux is calculated only for the invasion zone. The uninvaded/virgin zone is not considered.
(iv) The porosity of the formation follows Normal distribution.
(v) The virtual sonde consists of a source and detector that moves vertically along the borehole-axis (centered tool). The detector works at 100% efficiency. The source and the detector are 35 cm apart. The interval between two consecutive readings (of neutron flux) along the axis of the borehole is also 35 cm. The neutron source is considered to be of Ra-Be with $Q = 4.5 * 106 \,\text{neutrons}\,\text{s}^{-1}$.

2.1 Computer Program

In this work, a computer program in C++ has been created for computing the neutron flux (Φ) in the case of two concentric cylindrical mediums (see Eq. vi in the Appendix) and then used to generate the synthetic epithermal

neutron log. The computation of neutron flux also includes the computation of the Bessel function (Salvadori and Schwarz, 1956; Harper, 1976; Press et al., 1992). Fig. 2 presents the computation steps.

By appropriate calibration method, the neutron flux (expressed in count s^{-1}) is then converted to porosity values. To calibrate, the program is run assuming a constant porosity, and the corresponding count rate is obtained. This procedure is carried out for a number of porosities with different values of water saturation. The calibration curves are shown for sandstone and limestone in Figs. 3 and 4, respectively.

Comparison is made among a constant porosity, with particular water saturation, and other porosity values. In the case of limestone, the original porosity ranges 0.18–0.22, whereas for sandstone it is 0.29–0.31, at 100% water saturation for both rock types. The count rate is converted into porosities by using these calibration data. The derived porosity values are plotted versus depth to yield the synthetic neutron porosity logs for a number of models based on water and/or gas saturations. Figs. 5 and 6 show two cases of synthetic neutron porosity logs at 75% water saturation for sandstone and limestone, respectively. The distribution of the derived porosities is then compared to that of the original one.

Table 1 presents the different cases of water saturation models for sandstone and limestone. Tables 2 and 3 present the maximum, minimum, and average count rates, and their corresponding neutron porosity values for the different sandstone and limestone models. The mean and standard deviation of the derived porosity distribution is obtained (Table 4), which is then compared with the original porosity distribution (Table 4; Figs. 7 and 8).

2.2 Sandstone model

Fig. 5 presents the synthetic neutron porosity log for 75% water saturation model of sandstone (the remaining figures of other water saturation models, viz. 100%, 50%, and 35%, are with the authors). The shape of the logs much resemble those obtained in practical cases (such as in Serra, 1984; Nelson and Schimschal, 1993; Schlumberger Oilfield

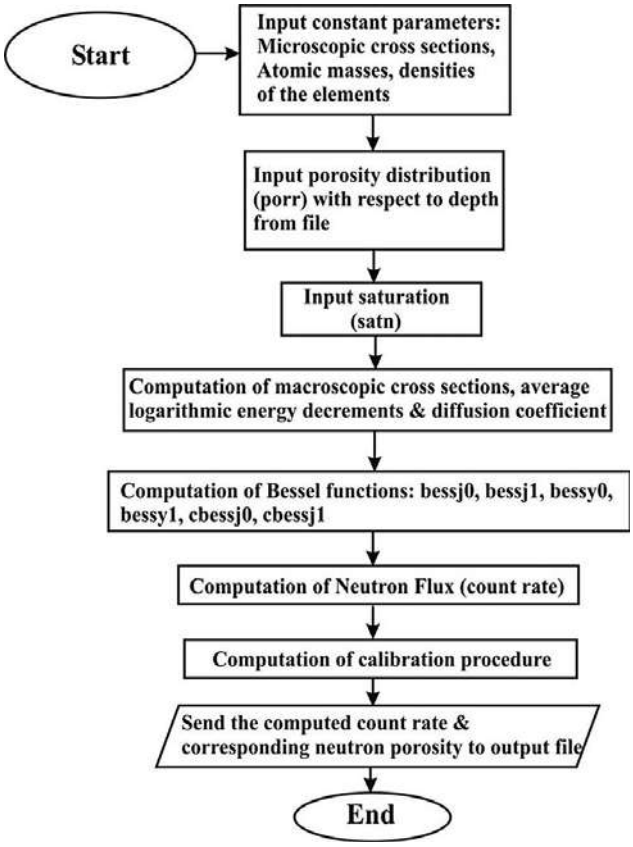

FIG. 2 Schematic flow chart diagram for computing neutron flux (count rate) and to get the corresponding neutron porosity values.

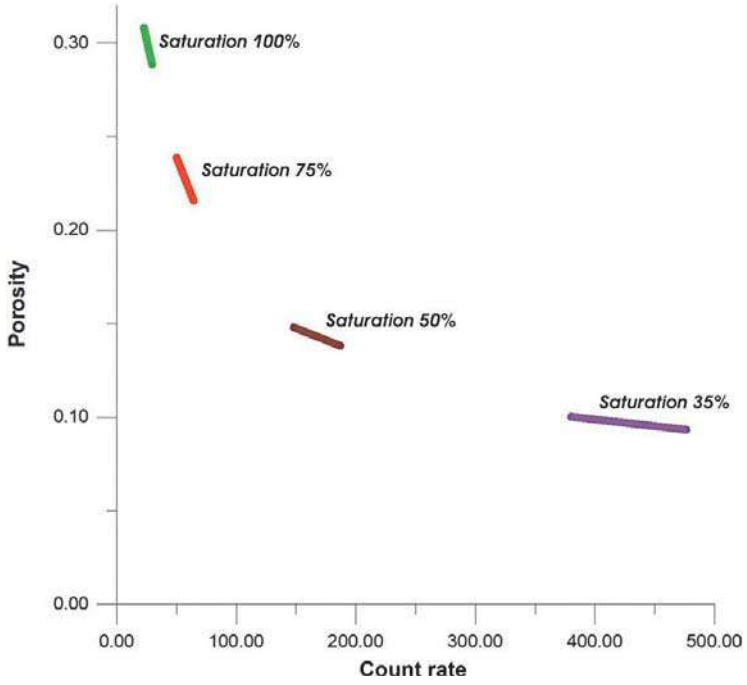

FIG. 3 Calibration curves for sandstone at different saturations.

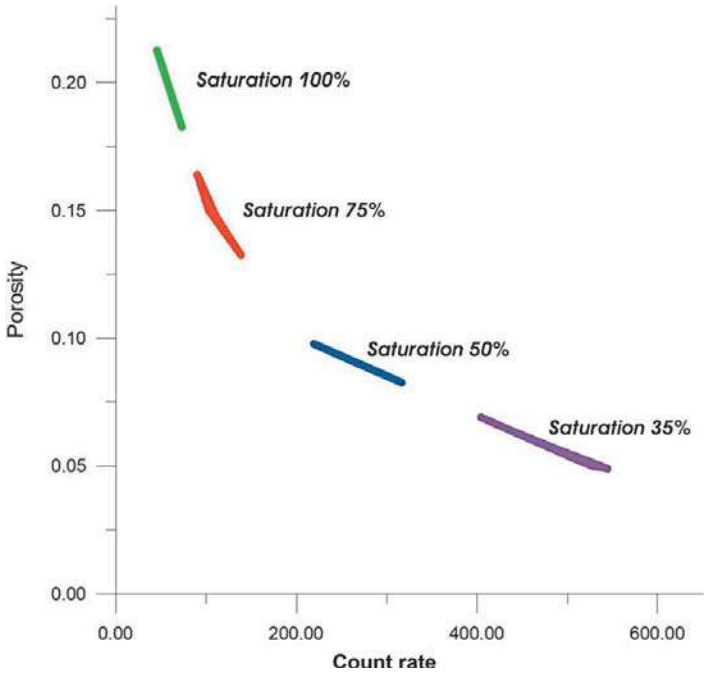

FIG. 4 Calibration curves for limestone at different saturations.

Review, 1994). Globally clean sandstones encountered in hydrocarbon reservoirs are comprised of predominantly quartz arenites, consisting of $\geq$95% quartz (Pettijohn, 1954; Dott, 1964; Pettijohn et al., 1987). The porosity distribution histograms of the original porosity model (i.e., the input porosity distribution) and that of the synthetic logs at different saturations are shown in Figs. 7 and 9, respectively. The derived porosity models compare well with the original, as revealed by the histograms showing normal distribution in Figs. 7 and 9.

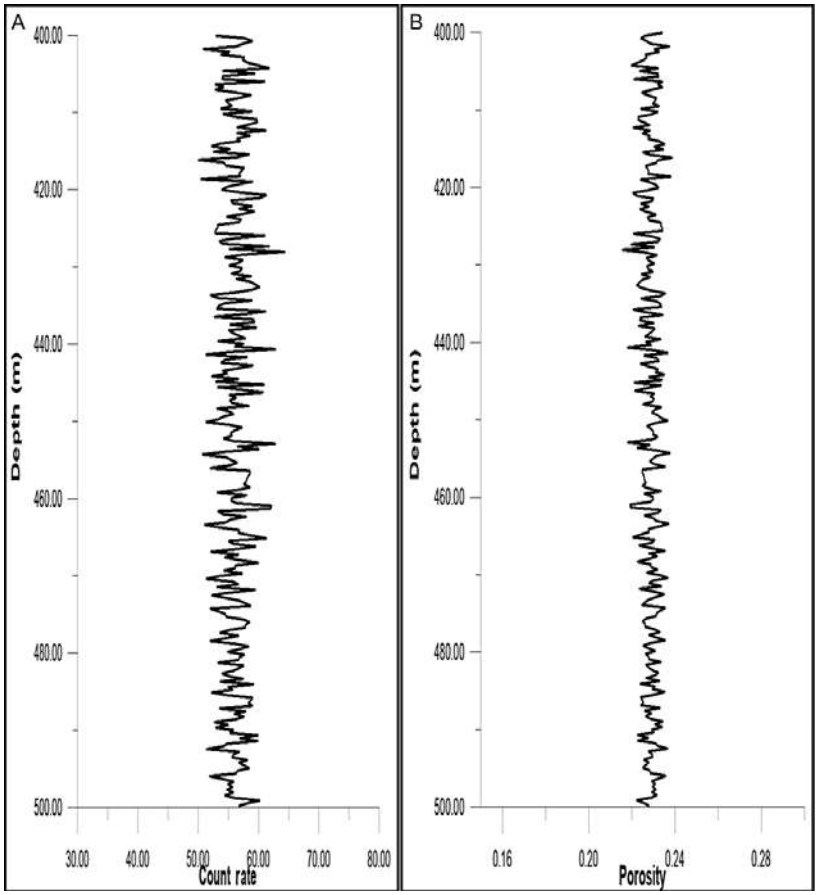

FIG. 5 Synthetic neutron log showing (A) count rate (SC2) versus depth and (B) porosity (S2) versus depth, in clean sandstone at 75% water saturation.

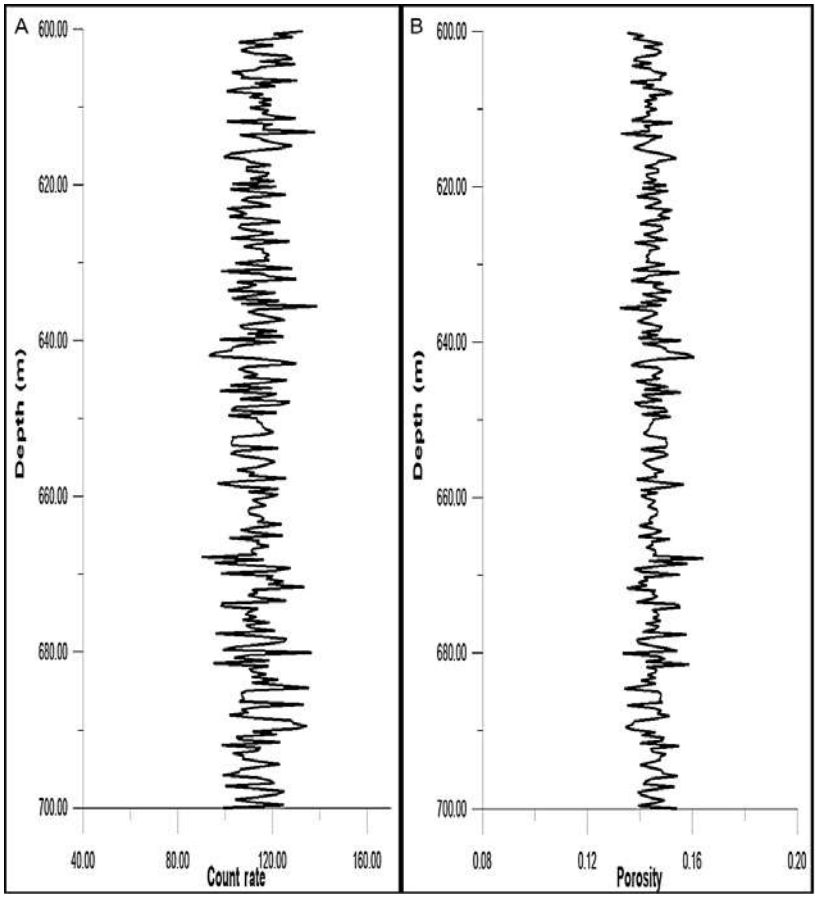

FIG. 6 Synthetic neutron log showing (A) count rate (LC2) versus depth, and (B) porosity (L2) versus depth, in clean limestone at 75% water saturation.

TABLE 1 Different Models of Sandstone and Limestone

Formation	Model number	Water saturation (%)	Gas saturation (%)
Sandstone	S1	100	0
	S2	75	25
	S3	50	50
	S4	35	65
Limestone	L1	100	0
	L2	75	25
	L3	50	50
	L4	35	65

TABLE 2 Maximum, Minimum, and Average Count Rates of the Different Models

			Count rate (neutrons/s)		
Formation	Model number	Water saturation (%)	Maximum	Minimum	Average
Sandstone	SC1	100	29	23	26
	SC2	75	64	54	56
	SC3	50	187	148	165
	SC4	35	476	380	422
Limestone	LC1	100	73	46	59
	LC2	75	139	90	114
	LC3	50	317	219	267
	LC4	35	618	450	533

TABLE 3 Minimum, Maximum, and Average Porosities of the Different Models

			Porosity		
Formation	Model number	Water saturation (%)	Minimum	Maximum	Average
Sandstone	S1	100	0.29	0.31	0.30
	S2	75	0.22	0.24	0.23
	S3	50	0.14	0.15	0.144
	S4	35	0.093	0.10	0.097
Limestone	L1	100	0.183	0.213	0.198
	L2	75	0.13	0.16	0.145
	L3	50	0.08	0.10	0.09
	L4	35	0.05	0.07	0.06

TABLE 4 Mean and Standard Deviation of the Derived and Original Models

				Porosity	
Formation	**Model number**	**Water saturation (%)**	**Gas saturation (%)**	**Mean**	**Standard deviation**
Sandstone	*Initial (original)*	100	0	0.30	0.0048
	S1	100	0	0.30	0.0034
	S2	75	25	0.23	0.0041
	S3	50	50	0.144	0.0017
	S4	35	65	0.097	0.0012
Limestone	*Initial (original)*	100	0	0.20	0.0073
	L1	100	0	0.198	0.0056
	L2	75	25	0.145	0.0049
	L3	50	50	0.09	0.0028
	L4	35	65	0.06	0.0046

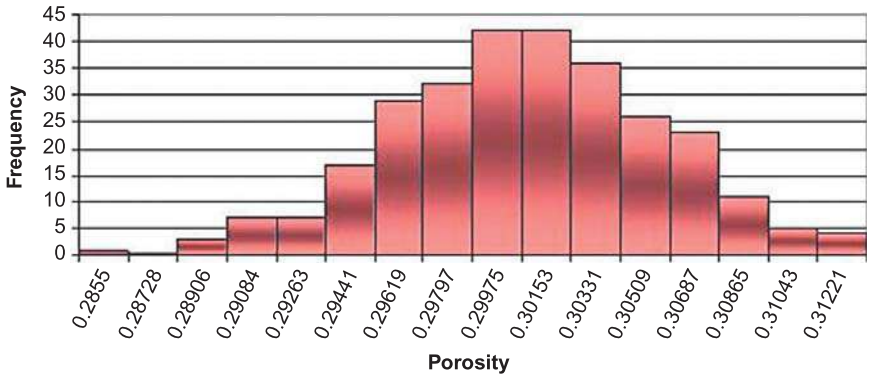

FIG. 7 Histogram of initial porosity distribution values in the case of sandstone model.

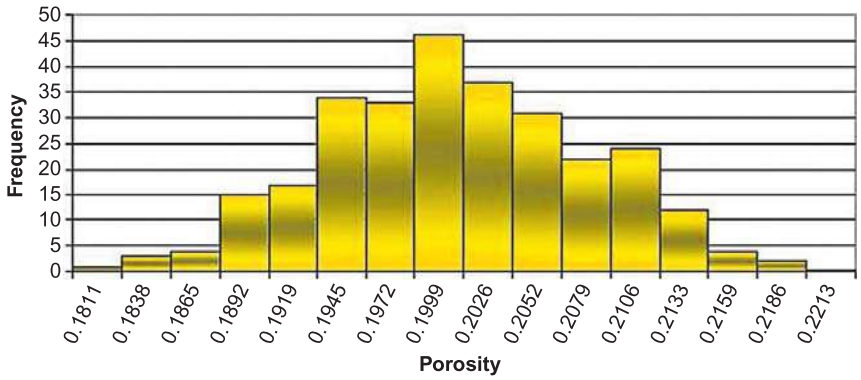

FIG. 8 Histogram of initial porosity distribution values in the case of limestone model.

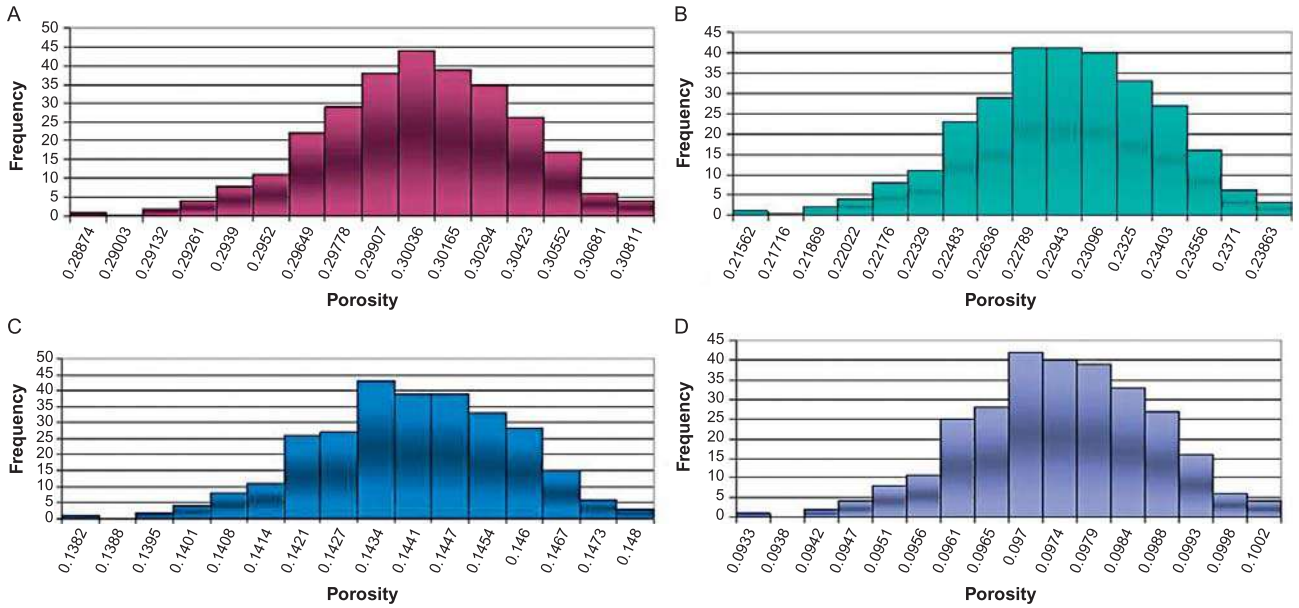

FIG. 9 Histograms of derived porosity values for sandstone models: (A) S1, (B) S2, (C) S3, and (D) S4.

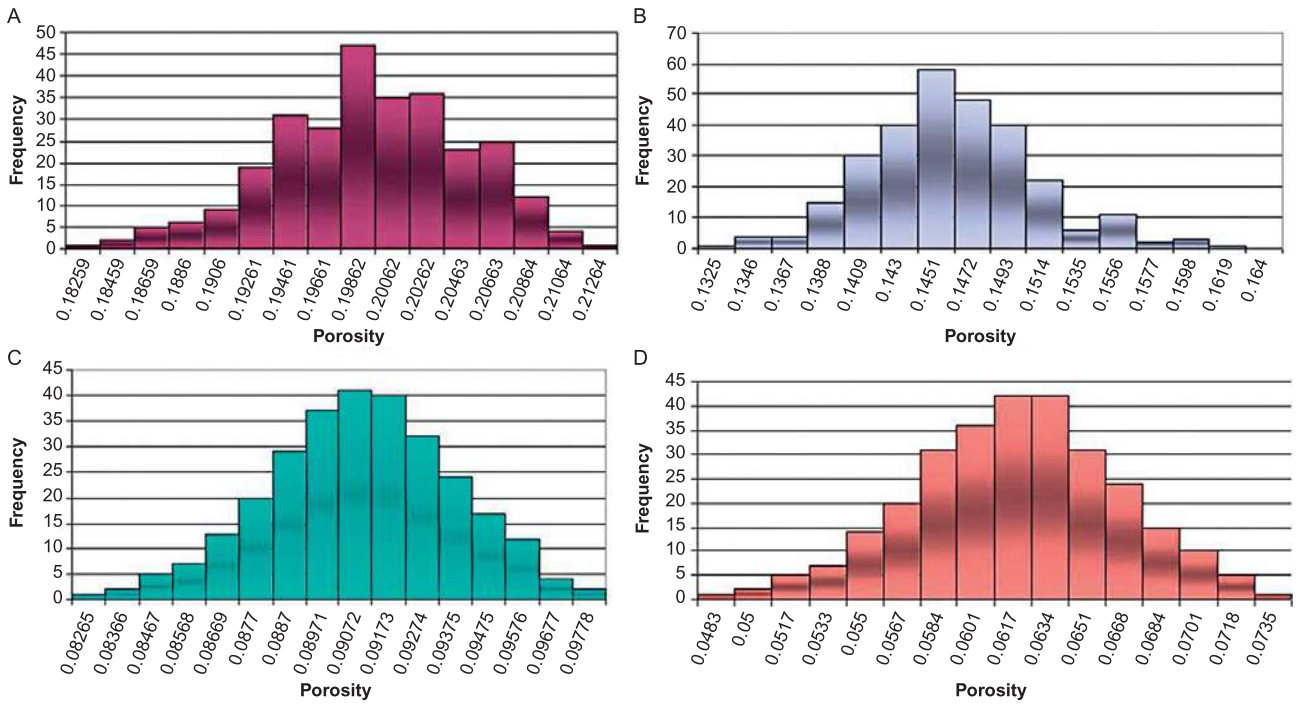

FIG. 10 Histograms of derived porosity values for limestone models: (A) L1, (B) L2, (C) L3, and (D) L4.

2.3 Limestone model

The synthetic neutron porosity log for 75% water saturation model of limestone is shown in Fig. 6 (the remaining figures of other water saturation models, namely 100%, 50%, and 35%, are with the authors). The shape of the logs is very much similar to those obtained in practical cases. The porosity distribution histograms of the original porosity model (i.e., the input porosity distribution) and that of the synthetic logs (at different saturations) are shown in Figs. 8 and 10, respectively. The derived porosity models seem to compare well with that of the original (Figs. 8 and 10) as revealed by the histograms showing normal distribution.

3 DISCUSSIONS

The numerical simulation used in this work is of deterministic type. The detector is supposed to be working at 100% efficiency. The result of the simulation is neutron flux (number of neutrons per second) obtained at number of points with varying depths. This has been converted to suitable porosity values to get the synthetic neutron logs for sandstone- and limestone models.

According to Figs. 3 and 4, the count rate decreases as water saturation increases. This is as expected as the number of hydrogen atoms, mainly responsible for slowing down of neutrons, increases with water saturation. Organic gases do not have sufficient hydrogen content in comparison to equivalent volume of water/oil, due to having lower densities. Figs. 5 and 6 and Tables 1–3 show the mode of neutron porosity change with variation of water saturation, in both sandstone and limestone. Thus with proper selection of the diffusion coefficient, the diffusion theory in concentric cylindrical medium can too be used for gas detection.

Because the maximum amount of energy loss is a function of a formation's hydrogen concentration, the Hydrogen Index (HI) of the formation fluid(s) controls the count rate observed by the neutron tool. The HI of a material is defined as the partial concentration of hydrogen per unit volume relative to water (see Elli and Singer, 2007). It is thus a proxy measure of porosity if the solid minerals of the formation matrix contain no hydrogen and if the pores are completely water-saturated. The HI of a material can be expressed as (Smolen, 1996):

$$\mathrm{HI} = \rho_b \times [(9 n_H A_H)/(\Sigma_i n_i A_i + n_H A_H)] \tag{6}$$

where n_H: the number of hydrogen atoms in a molecule of the material; A_H: the atomic mass of hydrogen atom in the material; n_i: the number of non-hydrogen atoms of element i in a molecule of the material; A_i: the atomic mass of non-hydrogen element i; ρ_b: density of the material. Note Mukherjee (2017, 2018a,b,c) for deducing representative density of a rock that shows continuous density variation in different directions.

Using Eq. (6), the hydrogen index of methane (CH_4) is:

$$\mathrm{HI_g} = 2.25 \times 0.00068 = 1.53 \times 10^{-3}. \tag{7}$$

Here, the density of CH_4 is taken to be $0.00068\,\mathrm{g\,cm^{-3}}$.

Hence as per the definition, the hydrogen index of pure water = 1.

Now, the effect of gas (CH_4) invasion on neutron porosity can be checked by using the following equation (Smolen, 1996):

$$\Phi_N = \Phi\left[\mathrm{HI_w} \times S_w + \mathrm{HI_g}(1 - S_w)\right] \tag{8}$$

where Φ_N: neutron porosity of the formation; Φ: actual (true) porosity of the formation; $\mathrm{HI_w}$: Hydrogen Index of water; $\mathrm{HI_g}$: Hydrogen Index of gas; and S_w: water saturation.

Hence using Eq. (8), one deduces the actual porosity of a formation from the neutron porosity.

Tables 5 and 6 reveal that the gas-corrected porosity comes close to the actual porosity with increase in water saturation. But overall, the gas corrected porosity magnitudes are close to that of the actual porosity.

The numerical simulation method adopted in this study generates good quality synthetic logs, and they resemble their original models. Both the initial and the final porosity models for sandstone and limestone are distributed normally. This is due mainly to the deterministic nature of the method of numerical simulation. The solution

TABLE 5 Neutron Porosity and Gas-Corrected Porosity for Sandstone Model

Formation	Model number	Water saturation (%)	Gas saturation (%)	Neutron porosity (average)	Porosity after gas correction (average)
Sandstone	S1	100	0	0.30	0.30
	S2	75	25	0.23	0.305
	S3	50	50	0.144	0.287
	S4	35	65	0.097	0.276

TABLE 6 Neutron Porosity and Gas-Corrected Porosity for Limestone Model

Formation	Model number	Water saturation (%)	Gas saturation (%)	Neutron porosity (average)	Porosity after gas correction (average)
Limestone	L1	100	0	0.198	0.198
	L2	75	25	0.145	0.193
	L3	50	50	0.09	0.181
	L4	35	65	0.06	0.174

of the diffusion equation is valid only for two concentric cylindrical systems, that is, for the borehole and the invasion zone. Note that the detection of neutrons has been assumed to be perfect; no actual detectors were modeled. Real detectors would be more complicated and their response depends on several other factors not considered here.

The spacing between neutron source and detector is considered constant in all cases (35 cm in the model). If this distance is increased, less number of epithermal neutrons gets captured at the detector, that is, the epithermal flux will be too small to obtain good statistics (Tittman et al., 1966; Serra, 1984; Schlumberger Log Interpretation Principles/Applications, 1989; Schlumberger Oilfield Review, 1994; Krygowski, 2003). For most eccentered epithermal neutron tools, the count rate "J" is proportional to slowing down length L_s. But, J is not directly proportional to L_s when gas fills up the pore space. In an actual scenario with epithermal neutron tools, this distance is ~40 cm. In the case of thermal neutron tools, the distance between source and detector may be $\geq$70 cm (Serra, 1984; Schlumberger Oilfield Review, 1994).

Like that of a gamma ray log, the density and neutron logs combined also act as a good lithology indicator apart from porosity detection. Another important log, which gives information about lithological features, is the borehole image log (e.g., Schlumberger Log Interpretation Principles/Applications, 1989; Gaillot et al., 2007). These images can be of electrical acoustics and video devices, and are obtained when the tool is lowered into the wellbore (Prensky, 1999; Asquith and Krygowski, 2004). The borehole image log, like the Formation Micro Imager (FMI, a Schlumberger proprietary), is commonly used to get high-resolution azimuthal coverage of the borehole, helpful in detection of reservoir heterogeneity related to fractures and secondary porosity (Hurley, 2004; Laongsakul and Dürrast, 2011). The FMI tool consists of a four-arm, eight-pad array, which sticks to the borehole wall and measures the electrical microresistivity in the flushed zone surrounding the borehole (Alizadeh et al., 2015). The resistivity data is subsequently converted into image form, where the darker features indicate less resistive and the lighter features are of more resistive beds/units/features. Thus in an image log, a fresh water- and/or hydrocarbon-bearing clean sandstone or carbonate body would be of lighter color (resistive body) whereas shale- and saline water-bearing sandstones would be of darker color (conductive). Any dipping body, fractures/bedding plane/lamination, appear as a half wavelength sinuous curve because the recording is done along the circumference of the borehole wall (Trice, 1999a,b; refer to Figs. 9.4, 9.7, and 9.8 in Hurley, 2004). Hence the natural fractures, bed boundaries, and laminations appear as arc-shaped features in an image log; the color of such features may vary from light to dark depending upon its material resistivity. These image logs provide crucial information about the reservoir structural elements such as folds, faults, unconformity, fractures (drilling induced, natural fractures), break outs, etc. (Trice, 1999a,b; Hurley, 2004; Dasgupta et al., in press). Other than structural features, image logs are also helpful in

understanding complex pore geometries (particularly secondary porosity) and facies variation that exists within a reservoir body predominantly in carbonates (Akbar et al., 1995; Chitale et al., 2009; Alizadeh et al., 2015; Zahmatkesh et al., 2015). The secondary porosities are not only related to vugs/caverns and grain leeching but also in many cases are linked to or generated by the natural fractures within a reservoir body (Trice, 1999a; Hurley, 2004; Bratton et al., 2006; Laongsakul and Dürrast, 2011).

3.1 Problem

The problems assigned here are related to practical applications of the aforesaid logs, that is, the neutron and image logs. The assigned Problem 1 defines the effect of gas in lowering neutron porosity in a clean porous sandstone body. Problem 2 is given to interpret an image log from a carbonate body to identify and distinguish the natural fractures and bed boundaries. Such natural fractures within carbonates aids in generating secondary porosity. The solutions are given in the Appendix.

(1) Find out the neutron porosity values at 14,610 ft. (4453.13 m) and 14,620 ft. (4456.18 m), respectively, within the gas saturated clean sandstone unit in Fig. 11. Obtain the actual porosity at these depths assuming that the gas saturated zone consists of only CH_4 and the gas saturations at 14,610 ft. and 14,620 ft. are ~0.90 and ~0.75, respectively.

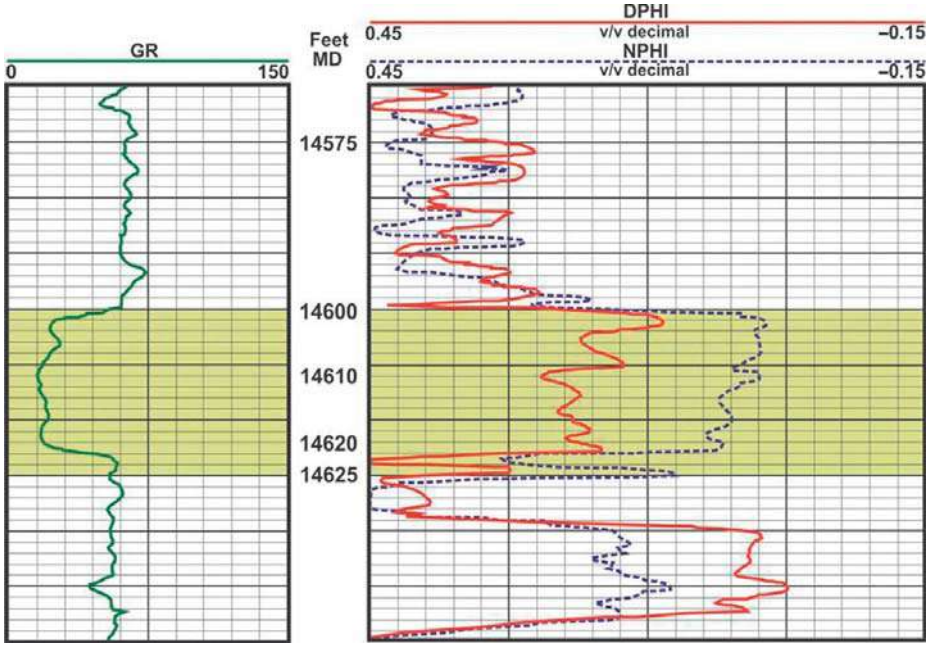

FIG. 11 Log of Atoka Sandstone, Permian Basin, USA Track 1 displays the gamma ray (GR). Track 2 shows neutron porosity (NPHI) and density porosity (DPHI). In the interval 14,600 ft. (4450.08 m) to 14,625 ft. (4457.7 m), comprising of clean sandstone (predominantly loose, coarse to very coarse, quartz arenite), high gas effect in the sandstone is observed in Track 2 by DPHI as well NPHI logs. Note that the density porosity reads a higher porosity value than that of neutron porosity in the gas-bearing zone. *Modified and partly reproduced from Asquith, G., Krygowski, D., 2004. Case study 1: Pennsylvanian Atoka sandstone, Permian Basin, U.S.A. In: Asquith, G., Krygowski, D., Henderson, S., Hurley, N. (Eds.), Basic Well Log Analysis: AAPG Methods in Exploration. second ed., vol. 16, pp. 168–179.*

(2) Identify the natural fractures and bed boundaries in the static image log data of Fig. 12.

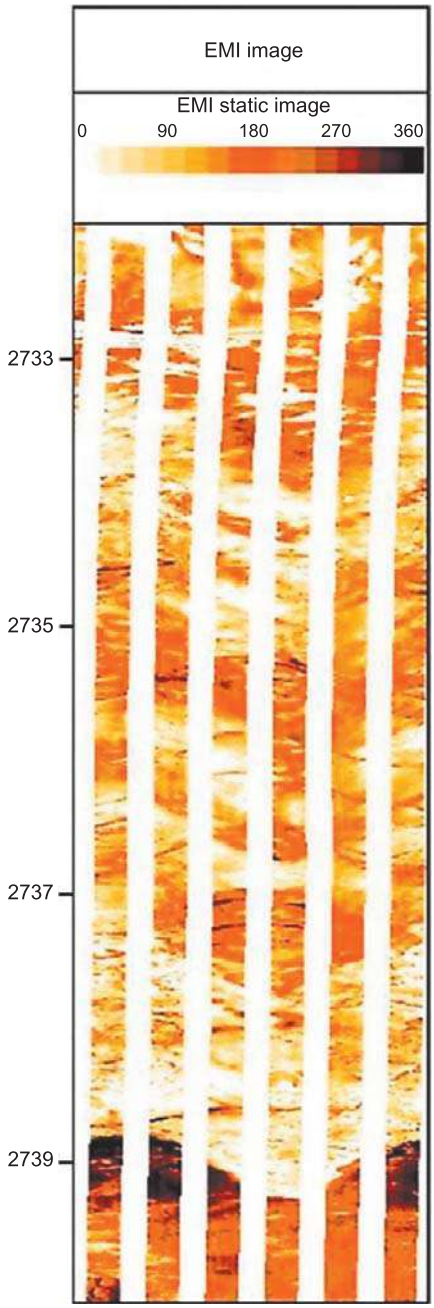

FIG. 12 Static image log data from a well in Aghajari carbonate field, Iran. The figure represents a resistivity image of cylindrical borehole wall in section view. Note that the lighter color indicates more resistive beds whereas the darker units are conductive beds. Thus there is lithological variation along depth, which is cut by numerous fractures. *Modified and partly reproduced from Vatandoust, M., Saein, A., 2018. Fracture analyses of fractured reservoir using static and dynamic data, case study: the Agharjari Oil Field (the Zagros Fold-Thrust Belt). In: Saein, A. (Ed.), Tectonic and Structural Framework of the Zagros Fold-Thrust Belt. Elsevier. ISBN: 978-0-12-815048-1.*

4 CONCLUSIONS

In the numerical study of an epithermal neutron log, the borehole is taken to be water-filled and devoid of mudcake. Environmental effects on the logs (Serra, 1984; Schlumberger Log Interpretation Principles/Applications, 1989) were not considered. If the borehole is taken to be mud-filled and the virgin zone also exists, the boundary conditions for another two cylindrical media require consideration. In spite of these simplifications in this work, the process of

neutron diffusion using one group diffusion theory for two concentric cylindrical media are simulated giving good results. The count rate should increase as water saturation falls, and this is displayed in this study. Note that as the count rate increases the corresponding neutron porosity falls.

An improved model with the mud-filled borehole with the presence of virgin zone should be considered for further 88study to match the real sub-surface logging scenarios. Moreover quite a lot of research was done on the advantages of epithermal neutron log in porosity determination during later part of 20th century. As a result of which oil service companies, during past few decades, now use the sidewall epithermal neutron logging tool (Tittman et al., 1966; Schlumberger Log Interpretation Principles/Applications, 1989) as well as nuclear magnetic resonance (NMR) logs, which have greater accuracy in resolving formation porosity both in clastic and carbonate lithology. Thus an integrated analysis of the porosity logs (neutron and density) as well as of other logs like sonic, nuclear magnetic resonance (NMR), and image log is required to have a better understanding of the reservoir porosity and permeability.

Supplementary data to this article can be found online at https://doi.org/10.1016/B978-0-12-814048-2.00019-3.

Acknowledgments

SDG's M.Tech. dissertation was with VNS. A CPDA grant and a research sabbatical for the year 2017 provided by IIT Bombay supported SM. Data shown in this work is of public domain; no data from Reliance Industries Ltd. have been used.

APPENDIX

A.1 Equation for Calculation of Neutron Flux

The flux for the inner medium (cylinder):

$$\Phi_{n1} = A_n J_0(C_n r) e^{-Fnz} \tag{i}$$

Here,

$$F_n = \sqrt{\left(C_n{}^2 + \left(1/L_1{}^2\right)\right)} \tag{ii}$$

The flux for the outer zone is:

$$\Phi_{n2} = G_n[J_0(P_n r) + H_n Y_0(P_n r)]e^{-Fnz} \tag{iii}$$

where

$$F_n = \sqrt{\left(P_n{}^2 + \left(1/L_2{}^2\right)\right)} \tag{iv}$$

J_0: Bessel function of first kind and zero order; Y_0: Bessel function of second kind and zero order.

H_n can be derived by using the boundary condition at $r = b$, i.e. $\Phi_{n2} = 0$. This gives,

$$H_n = -[J_0(P_n b)/Y_0(P_n b)] \tag{v}$$

Thus by solving the other boundary conditions, the total flux in case of concentric cylinder is (Tittle, 1961):

$$\Phi_{n2} = \Sigma_n G_n[J_0(P_n r) + H_n Y_0(P_n r)]e^{-Fnz} \tag{vi}$$

This is the derivation of neutron flux for concentric cylindrical system in a real logging situation (Tittle, 1961).

Φ_{n2}/Φ_n: neutron flux (number of neutrons cm^{-2} s^{-1}) for two concentric cylinders; J_0 = Bessel function of first kind and zero order; Y_0 = Bessel function of second kind and zero order.

$F_n = [P_n^2 + L_2^{-2}]^{0.5}$ (L_2 = slowing down length for the second medium; i.e., the outer cylinder, i.e., representing the invasion zone in real scenario).

$$H_n = -[J_0(P_n b)/Y_0(P_n b)]. \tag{vii}$$

P_n (in Eq. vii) and C_n (in Eq. i) can be obtained by solving:

$$\left[D_2 J_0(y)/D_1 y J_1(y)\right] = [J_0(x) - \{J_0(kx)Y_0(x)/Y_0(kx)\}]/x[J_1(x) - \{J_0(kx)Y_1(x)/Y_0(kx)\}] \tag{viii}$$

or,

$$[D_2 g(y)/D_1] = f(x) \tag{ix}$$

Here,

$$x = P_n a \tag{x}$$

$$y = C_n a = \sqrt{\left[x^2 + \left(a^2/{L_2}^2\right) - \left(a^2/{L_1}^2\right)\right]} \tag{xi}$$

$$k = b\,a^{-1}$$

J_1: Bessel function of first kind and first order; Y_1 = Bessel function of second kind and first order; L_1: Slowing down length for the first medium (borehole); L_2: Slowing down length for the second medium (invasion zone); D_1: Neutron diffusion coefficient in case of the first medium (borehole); D_2: Neutron diffusion coefficient in case of the second medium (invasion zone).

Eq. (viii) is solved for "x" numerically. The functions are then graphed as functions of x and the points of intersection give the values of the roots, x_n.

G_n (of Eq. vi) is derived from:

$$C_n A_n D_1 J_1(C_n a) = P_n G_n D_2 [J_1(P_n a) + H_n Y_1(P_n a)] \tag{xii}$$

And is obtained from:

$$A_n = Q/\left[2\pi D_1 F_n a^2 U_n B_n\right] \tag{xiii}$$

Here

$$B_n = \left[{J_0}^2(y_n) + {J_1}^2(y_n) + (D_2/D_1)\{J_0(y_n)/Z_0(x_n)\}^2 \times \left\{k^2 {Z_1}^2(kx_n) - {Z_0}^2(x_n) - {Z_1}^2(x_n)\right\}\right] \tag{xiv}$$

$$U_n = [[J_1(y_n) + \{D_2 y_n J_0(y_n)/D_1 x_n Z_0(x_n)\} \times \{kZ_1(kx_n) - Z_1(x_n)\}]/ \left[J_1(y_n) + \left(\sqrt{D_2/D_1}\right) \times \{y_n J_0(y_n)/x_n Z_0(x_n)\} \times \{kZ_1(kx_n) - Z_1(x_n)\}\right]] \tag{xv}$$

Here,

$$Z_0(x) = J_0(x) + H_n Y_0(x) \tag{xvi}$$

$$Z_1(x) = J_1(x) + H_n Y_1(x) \tag{xvii}$$

$$F_n = \left[{C_n}^2 + \left(1/{L_1}^2\right)\right]^{0.5} = \left[{P_n}^2 + {L_2}^{-2}\right]^{0.5} \tag{xviii}$$

$$H_n = -[J_0(kx)/Y_0(kx)]\ [\text{refer to Eq. (vii)}] \tag{xix}$$

A.2 Imaginary Arguments of the Bessel Function

While solving Eq. (xi) for C_n, instances arise in which C_n is imaginary. This is because usually $L_1 < L_2$, and thus y will be imaginary. Let $y = iu$, where $i = \sqrt{(-1)}$ and u is real. These cases of imaginary C_n has been included in the analysis, because $J_0(iu)$ is a real function. Note although $J_1(iu)$ is imaginary, it is observed from Eq. (viii) that, as a product with iu, the combination becomes real.

A.3 Computation of the Neutron Flux (Φ)

In the present deterministic simulation, the flux is computed using Eq. (vi). The neutron source considered is of Ra-Be with neutron flux, $Q = 4.5 \times 10^6$ neutrons s^{-1}. Table A1 presents magnitudes of atomic mass, scattering (epithermal level), and absorption cross-section, and the average logarithmic energy decrement of the required elements. Computations of all the parameters that appear in the Eq. (vi) are described later.

A.4 Computation of P_n and C_n

Eq. (viii) is solved for "x" by numerical methods using C++ programming. The functions are then graphed as functions of x and the points of intersection give the values of the roots, x_n (Fig. A1). These x_n values (Table A2) are used to compute neutron flux in the case of two concentric cylindrical media. If "k" is not large enough (< 10), it is sufficient to

TABLE A1 Neutron Properties of Some Elements Encountered in Logging (Liverhant, 1960)

Elements	Atomic mass	Absorption cross-section (σ_a-in barns) (1b = 10^{-24} cm^2)	Scattering cross-section (σ_s-in barns) (epithermal) (1b = 10^{-24} cm^2)	Average logarithmic energy decrement (ξ)
Hydrogen (H)	1	0.332	20.4	1.0
Oxygen (O)	16	0.00019	3.75	0.12
Silicon (Si)	28	0.16	2.2	0.070
Carbon (C)	12	0.0034	4.66	0.15
Calcium (Ca)	40	0.44	3.0	0.049

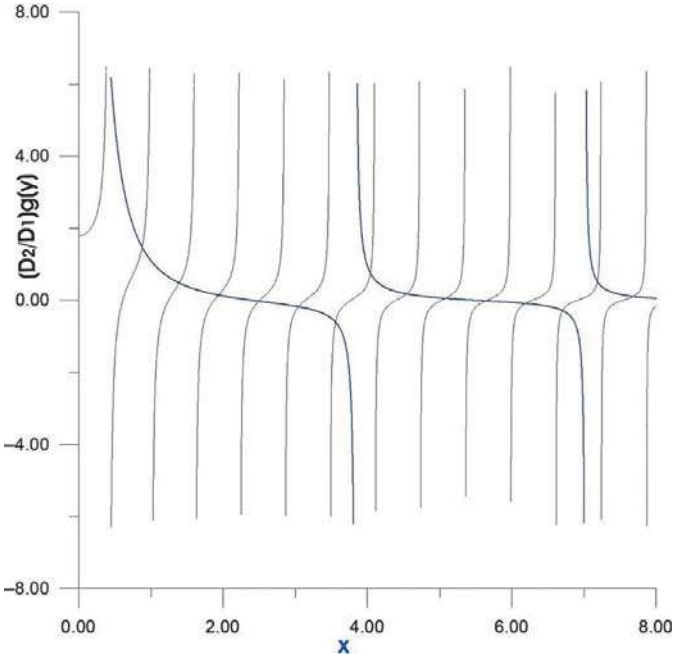

FIG. A1 Graphical method for finding the roots (x_n) from Eqs. (viii) and (ix). The light curve represents $f(x)$ whereas the dark blue curve is $D_2 g(y)/D_1$.

TABLE A2 Values of the Roots, x_n, Corresponding to each n

n	1	2	3	4	5	6	7	8	9	10	11	12
x_n	0.8773	1.3906	1.936	2.494	3.0426	3.5576	4.0393	4.5399	5.0797	5.6364	6.1856	6.7022

consider the first 10 terms of the series (Tittle, 1961). The cases are for a 6-in. diameter water-filled borehole in water-saturated limestone with high (30%) porosity. Here $k = 6$ and $D_2\, D_1^{-1} = 0.63$.

A.5 Computation of Neutron Diffusion Coefficient (D)

The neutron diffusion coefficient, D, is (Glasstone and Edlund, 1957; Liverhant, 1960; Lamarsh, 1983; Stacey, 2001):

$$D = L_s^2 \xi \Sigma \tag{xx}$$

where L_s: neutron slowing down length; ξ: Average logarithmic energy decrement; Σ: Macroscopic cross section. Thus to calculate D, ξ, Σ and L_s are to be computed.

A.6 Computation of Macroscopic Cross-section (Σ)

The total macroscopic cross-section in the case of clean water-saturated sandstone (i.e., composed of SiO_2 and H_2O) can be computed in the following manner.

Total macroscopic scattering cross-section for H_2O:

$$\Sigma_s H2O : \rho \times A_v(2 \times \sigma_{sH} + \sigma_{sO})/M \tag{xxi}$$

where Σ_{sH2O}: macroscopic scattering cross section of H_2O; ρ: density of water; A_v: Avogadro's number; M: molecular weight of water (H_2O).

The same procedure is involved for calculating the absorption cross-section for water:

$$\Sigma_{aH2O} = \rho \times A_v(2 \times \sigma_{aH} + \sigma_{aO})/M \tag{xxii}$$

where Σ_{aH2O}: macroscopic absorption cross section of H_2O; ρ: density of water (H_2O); A_v: Avogadro's number; M: molecular weight of water (H_2O).

Thus the total macroscopic cross-section of water is:

$$\Sigma_{H2O} = \Sigma_{sH2O} + \Sigma_{aH2O} \tag{xxiii}$$

where Σ_{H2O}: Total macroscopic cross-section of H_2O; Σ_{sH2O}: Macroscopic scattering cross-section of H_2O; Σ_{aH2O}: Macroscopic absorption cross-section of H_2O.

Similarly the calculation of total macroscopic cross-section of SiO_2 involves:

$$\Sigma_{SiO2} = \Sigma_{sSiO2} + \Sigma_{aSiO2} \tag{xxiv}$$

where Σ_{SiO2}: total macroscopic cross-section of SiO_2; Σ_{sSiO2}: macroscopic scattering cross-section of SiO_2; Σ_{aSiO2}: macroscopic absorption cross-section of SiO_2.

Similarly the total macroscopic cross-section for $CaCO_3$ and H_2O are computed for saturated limestone formation. The mean-free path (λ) can be calculated from Σ by the following equation:

$$\lambda = \Sigma^{-1} \tag{xxv}$$

A.7 Computation of Average Logarithmic Energy Decrement (ξ)

Neutrons continuously lose their energy while interacting with different nuclei in the formation medium. The calculation of average logarithmic energy decrement for a particular element can be performed by (Hearst et al., 2000):

$$\xi = \ln(E \cdot/E) = 1 + \left[(A-1)^2/2A\right] \ln\{(A-1)/(A+1)\} \tag{xxvi}$$

where ξ: Average logarithmic energy decrement; $E./E$: Ratio of the initial energy $E.$ to final energy E; A: Mass number of element.

ξ is evaluated at the final epithermal energy E. The previous calculation applies to individual elements. But the neutrons interact with the bulk medium and thus to calculate the average logarithmic energy decrement for clean formation (sandstones and limestones) media, the computation would be:

(i) Clean sandstone with pore spaces completely filled with water:

$$\xi_{sst} = \xi_H f_H + \xi_O f_O + \xi_{Si} f_{Si} \tag{xxvii}$$

where ξ_{sst}, ξ_H, ξ_O: average logarithmic energy decrement of sandstone, H and SI, respectively; ξ_{Si}: Average logarithmic energy decrement of Si; f_H, f_O, f_{Si}: fraction of H, O and Si atoms, respectively, with respect to the total number of atoms.

(ii) Clean limestone with pore spaces partially filled with water and gas (CH_4):

$$\xi_{lst} = \xi_{Ca} f_{Ca} + \xi_O f_O + \xi_C f_C + \xi_H f_H \tag{xxviii}$$

where ξ_{lst}: average logarithmic energy decrement of limestone; ξ_H, ξ_O, ξ_{Ca}, ξ_C: average logarithmic energy decrement of H, O, Ca and C, respectively; f_H, f_O, f_{Ca}, f_C: fraction of H, O, Ca and C atoms, respectively, with respect to the total number of atoms.

A.8 Computation of Slowing Down Length (L_s)

In neutron logging, the slowing down length L_s is (Allen et al., 1966; Neuman et al., 1988; Hearst et al., 2000):

$$L_s = (r^2/6)^{0.5} \tag{xxix}$$

where R: rms crow-flight distance a neutron travels from the source to the point where it reaches the energy of interest. Thus the slowing down length in a formation or a scattering material is the average distance a neutron travels before its energy reduces to an appropriate level. Typical values of L_s as a function of porosity are shown in Fig. 1 of Neuman et al. (1988) for limestone, sandstone, and dolomite formation saturated with fresh water. These values are taken for computational purpose.

A.9 Solutions of Problems Stated in Discussions Paragraph

1. The neutron porosity value at 14,610 ft. is 0.03 and at 14,620 ft. is 0.07. The actual or gas-corrected porosity is derived using Eq. (8). Accordingly, the actual porosities at 14,610 ft. and 14,620 ft. are 0.296% or 29.6% and 0.279% or 27.9%, respectively.
2. The interpretation of Fig. 12 is given in Fig. A2.

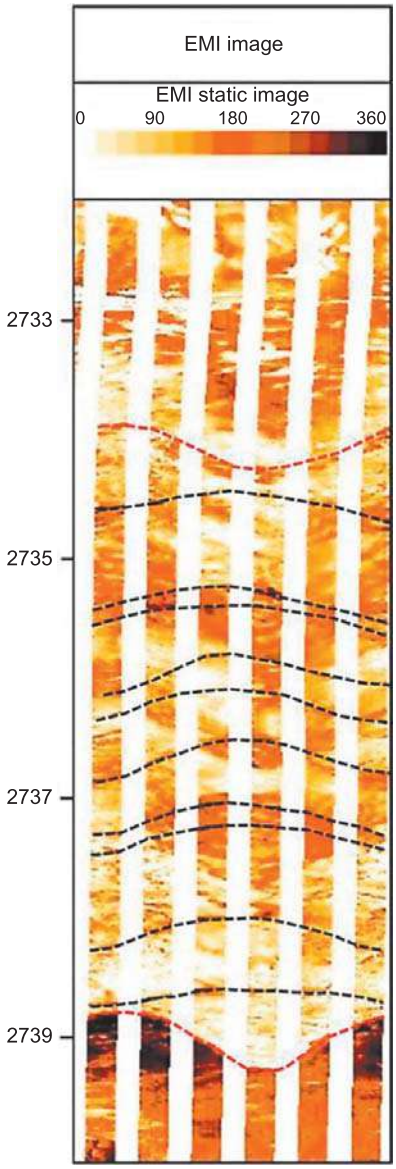

FIG. A2 Interpreted static image log data. The red dashed line depicts bed/lithological boundaries whereas the black dashed line depicts natural fractures. The orientation of the fracture planes and the bedding planes/lithological boundaries are not parallel, rather they cross-cut each other. *Modified and partly reproduced from Vatandoust, M., Saein, A., 2018. Fracture analyses of fractured reservoir using static and dynamic data, case study: the Agharjari Oil Field (the Zagros Fold-Thrust Belt). In: Saein, A. (Ed.), Tectonic and Structural Framework of the Zagros Fold-Thrust Belt. Elsevier. ISBN: 978-0-12-815048-1.*

These problems deal with the practical purpose of interpretation of log data. Problem 1 defines the effect of gas saturation on neutron log response whereas Problem 2 is given to identify natural fractures and bed boundaries from an image log.

Supplementary figures and captions (Figs. S1–S6 in the online version at https://doi.org/10.1016/B978-0-12-814048-2.00019-3) will be displayed in: http://www.geos.iitb.ac.in/index.php/en/sm-publications.

References

Akbar, et al., 1995. Classic Interpretation Problems: Evaluating Carbonates. Schlumberger Oilfield Review.

Alizadeh, M., Movahed, Z., Junin, R.B., 2015. Porosity analysis using image logs. Environ. Sci. 10, 326–337.

Allen, L.S., Tittle, C.W., 1964. Some functions in the theory of neutron logging. J. Grad. Res. Center South. Method. Univ. 33, 33–54.

Allen, L.S., Tittle, C.W., Mills, W.R., Caldwell, R.L., 1966. Dual-spaced neutron logging for porosity. Geophysics XXXII, 60–68.

Anovitz, L.M., Cole, D.R., 2015. Characterization and analysis of porosity and pore structures. Rev. Mineral. Geochem. 80, 61–164.

Asquith, G., Krygowski, D., 2004. Case study 1: Pennsylvanian Atoka sandstone, Permian Basin, U.S.A. In: Asquith, G., Krygowski, D., Henderson, S., Hurley, N. (Eds.), Basic Well Log Analysis: AAPG Methods in Exploration, second ed. 16, pp. 168–179, Oklahoma.

Bansal RS, Kumar A, Chawla S, Rana SP, Chakravorty RN, 2004 Understanding of reservoir heterogeneity and its impact on flow Behaviour to facilitate improve recovery in a mature carbonate reservoir: An example from Western Offshore Basin, India, AAPG International Conference: Cancun, Mexico.

Bratton, et al., 2006. The Nature of Naturally Fractured Reservoirs. Schlumberger Oilfield Review.

Burruss, R C, and Ryder, R T, 2003. Composition of crude and natural gas produced from 14 wells in the lower Silurian Clinton sandstone and Medina Group; NE Ohio and NW Pennsylvania, USGS Report (internal) Virginia.

Chitale, D.V., Johnson, C., Manley, H., Entzminger, D., Cante, L., 2009. Application of Borehole Imaging to Evaluate Porosity and Permeability in Carbonate Reservoirs: From Example from Permian Basin. In: AAPG Annual Convention. TX, San Antonio.

Dasgupta, T., Dasgupta, S., Mukherjee, S., in press. Image log interpretation of geomechanical issues. In: Mukherjee, S. (Ed.), Teaching Methodologies in Structural Geology and Tectonics. Springer. ISBN 978-981-13-2781-0.

Dott, R.H., 1964. Wacke, greywacke and matrix; what approach to immature sandstone classification? SEPM J. Sediment. Res. 34, 625–632.

Elli, D.V., Singer, J.M., 2007. Well Logging for Earth Scientists, second ed. Springer, Netherlands, pp. 351–392.

Fitch, P., Davies, S., Lovell, M., Pritchard, T., 2013. Reservoir Quality and Reservoir Heterogeneity: Petrophysical Application of the Lorenz Coefficient. Society of Petrophysicists and Well-Log Analysts (SPWLA), p. 54.

Gaillot, P., Brewer, T., Pezard, P., Yeh, E.-C., 2007. Borehole imaging tools—principles and applications. Sci. Drill. 5, 1–4.

Glascock, M.D., 2006. An Overview of Neutron Activation Analysis. The University of Missouri Research Reactor Center, Columbia.

Glasstone, S., Edlund, M.C., 1957. The Elements of Nuclear Reactor Theory. McMillan and Co. Ltd., London, pp. 98–107 and 208–213.

Harper, C., 1976. Introduction to Mathematical Physics. Prentice Hall India Pvt. Ltd, New-Delhi, pp. 189–200.

Hearst, J.R., Nelson, P.H., Paillet, F.L., 2000. Well Logging for Physical Properties, second ed. John Wiley & Sons, Ltd., pp. 196–215.

Hurley, N., 2004. Borehole images. In: Asquith, G., Krygowski, D. (Eds.), Basic Well Log Analysis. AAPG Methods in Exploration, second ed. 16, pp. 151–163.

Krygowski, D.A., 2003. Guide to Petrophysical Interpretation. Austin, TX.

Lamarsh, J.R., 1983. Introduction to Nuclear Reactor Theory, second ed. Addison-Wesley, Reading, MA.

Laongsakul, P., Dürrast, H., 2011. Characterization of reservoir fractures using conventional geophysical logging. Songklanakarin J. Sci. Technol. 33 (2), 237–246.

Liverhant, S.E., 1960. Elementary Introduction to Neutron Reactor Physics. John Wiley & Sons, New York. pp. 410–413 & 424–426.

Lynch, E.J., 1962. Formation Evaluation. Harper and Row Publishers, New York, pp. 249–255.

Mukherjee, S., 2017. Airy's isostatic model: a proposal for a realistic case. Arab. J. Geosci. 10, 268. https://doi.org/10.1007/s12517-017-3050-9.

Mukherjee, S., 2018a. Locating center of pressure in 2D geological situations. J. Ind. Geophys. Union 22, 49–51.

Mukherjee, S., 2018b. Locating center of gravity in geological contexts. Int. J. Earth Sci. https://doi.org/10.1007/s00531-017-1560-z.

Mukherjee, S., 2018c. Moment of inertia for rock blocks subject to bookshelf faulting with geologically plausible density distributions. J. Earth Syst. Sci. 127, 80. https://doi.org/10.1007/s12040-018-0978-4.

Nelson, P.H., Schimschal, U., 1993. Assessment of Geophysical Logs from Borehole USW G-2, Yucca Mountain, Nevada; Nevada Field Office. U.S. Department of Energy, Colorado.

Neuman, C.H., Salaita, G.N., Mahdavi, M., 1988. Neutron scattering for porosity determination. IEEE Trans. Nucl. Sci. 35, 812–815.

Pettijohn, F.J., 1954. Classification of sandstones. J. Geol. 62 (4), 360–365.

Pettijohn, F.J., Potter, P.E., Siever, R., 1987. Sand and Sandstone. Springer-Verlag, New York.

Pranter, M.J., Reza, Z.A., Budd, D.A., 2006. Reservoir-scale characterization and multiphase fluid flow modelling of lateral petrophysical heterogeneity within dolomite facies of the Madison formation, sheep Canyon and Lysite Mountain, Wyoming, USA. Pet. Geosci. 12, 29–40.

Prensky, S., 1999. Advances in borehole imaging technology and applications. In: Lovell, M.A., Williamson, G., Harvey, P.K. (Eds.), Borehole Imaging: Applications and Case Histories. Geological Society, London, pp. 1–44. Special Publications 159.

Press, W.H., Teukolsky, S.A., Vetterling, W.T., Flannery, B.P., 1992. Numerical Recipes in C, second ed. Cambridge University Press, Cambridge, pp. 230–234.

Salvadori, M.G., Schwarz, R.J., 1956. Differential Equations in Engineering: Problems. Prentice Hall, Inc., pp. 295–313.

Schlumberger Log Interpretation Principles/Applications, 1989. Schlumberger Ltd., Houston, TX, pp. 5–17 to 5–23.

Schlumberger Oilfield Review, October 1994. Neutron Porosity Logging Revisited, Internet ref: https://www.slb.com/~/media/Files/resources/oilfield_review/ors94/1094/p04_08.pdf. (accessed on 13-July-2017).

Serra, O., 1984. Fundamentals of Well Log Interpretation—The Acquisition of Logging Data. Development of Petroleum Science 15A. Elsevier, Amsterdam.

Singhal BBS, Gupta RP, 2010. Applied Hydrogeology of Fractured Rocks. Springer Science, p. 13–33. ISBN: 978-90-481-8798-0.

Smolen, J.J., 1996. Cased Hole and Production Log Evaluation. PennWell Books, Tulsa, Okla, pp. 214–218.
Stacey, W.M., 2001. Nuclear Reactor Physics. John Wiley & Sons. ISBN: 0-471-39127-1.
Tittle, C.W., 1961. Theory of neutron logging 1. Geophysics 26, 27–39.
Tittle, C.W., Allen, L.S., 1966. Theory of neutron logging 2. Geophysics 31, 214–224.
Tittman, J., Sherman, H., Nagel, W.A., 1966. The sidewall epithermal neutron porosity log. Soc. Petrol. Eng 18 (10), 1351–1362. https://doi.org/10.2118/1180-PA.
Trice, R., 1999a. A methodology for applying a non-unique, morphological classification to sine wave events picked from borehole image log data. In: Lovell, M.A., Williamson, G., Harvey, P.K. (Eds.), Borehole Imaging: Applications and Case Histories. Geological Society, London, pp. 77–90. Special Publications 159.
Trice, R., 1999b. Application of Borehole Image Logs in Constructing 3D Static Models of Productive Fracture Networks in the Apulian Platform, Southern Apennine. In: Lovell, M.A., Williamson, G., Harvey, P.K. (Eds.), Borehole Imaging: Applications and Case Histories. Geological Society, London, pp. 155–176. Special Publications 159.
Yang S, 2017. Natural Gas Physical Properties under High Pressure in Fundamentals of Petrophysics. Chapter 2, Springer Mineralogy, Germany, p. 27–74.
Zahmatkesh, I., Aghli, G., Mohamadian, R., 2015. Systematic fractures analysis using image logs and complementary methods in the Marun Oilfield, SW Iran. Geopersia 5 (2), 139–150.

Further Reading

Vatandoust, M., Saein, A., 2018. Fracture analyses of fractured reservoir using static and dynamic data, case study: the Agharjari Oil Field (the Zagros Fold-Thrust Belt). In: Saein, A. (Ed.), Tectonic and Structural Framework of the Zagros Fold-Thrust Belt. Elsevier. 978-0-12-815048-1.